BIOCHEMISTRY
including biophysical chemistry & molecular biology
Article

Biochemistry **2010,** *49,* 10803–10810 10803
DOI: 10.1021/bi1013479

Role of Zinc in Isoform-Selective Inhibitor Binding to Neuronal Nitric Oxide Synthase[†,‡]

Silvia L. Delker,[§] Fengtian Xue,[∥,⊥] Huiying Li,[§] Joumana Jamal,[§] Richard B. Silverman,*[,∥] and Thomas L. Poulos*[,§]

[§]*Departments of Molecular Biology and Biochemistry, Pharmaceutical Sciences, and Chemistry, University of California, Irvine, California 92697-3900, United States, and* [∥]*Department of Chemistry, Department of Molecular Biosciences, Center for Molecular Innovation and Drug Discovery, and Chemistry of Life Processes Institute, Northwestern University, 2145 Sheridan Road, Evanston, Illinois 60208-3113, United States.* [⊥]*Current address: Department of Chemistry, University of Louisiana, Lafayette, LA 70504.*

Received August 19, 2010; Revised Manuscript Received October 28, 2010

ABSTRACT: In previous studies [Delker, S. L., et al. (2010), *J. Am. Chem. Soc. 132*, 5437−5442], we determined the crystal structures of neuronal nitric oxide synthase (nNOS) in complex with nNOS-selective chiral pyrrolidine inhibitors, designed to have an aminopyridine group bound over the heme where it can electrostatically interact with the conserved active site Glu residue. However, in addition to the expected binding mode with the (*S*,*S*)-*cis* inhibitors, an unexpected "flipped" orientation was observed for the (*R*,*R*)-*cis* enantiomers. In the flipped mode, the aminopyridine extends out of the active site where it interacts with one heme propionate. This prompted us to design and synthesize symmetric "double-headed" inhibitors with an aminopyridine at each end of a bridging ring structure [Xue, F., Delker, S. L., Li, H., Fang, J., Jamal, J., Martásek, P., Roman, L. J., Poulos, T. L., and Silverman, R. B. Symmetric double-headed aminopyridines, a novel strategy for potent and membrane-permeable inhibitors of neuronal nitric oxide synthase. J. Med. Chem. (submitted for publication)]. One aminopyridine should interact with the active site Glu and the other with the heme propionate. Crystal structures of these double-headed aminopyridine inhibitors in complexes with nNOS show unexpected and significant protein and heme conformational changes induced by inhibitor binding that result in removal of the tetrahydrobiopterin (H_4B) cofactor and creation of a new Zn^{2+} site. These changes are due to binding of a second inhibitor molecule that results in the displacement of H_4B and the placement of the inhibitor pyridine group in position to serve as a Zn^{2+} ligand together with Asp, His, and a chloride ion. Binding of the second inhibitor molecule and generation of the Zn^{2+} site do not occur in eNOS. Structural requirements for creation of the new Zn^{2+} site in nNOS were analyzed in detail. These observations open the way for the potential design of novel inhibitors selective for nNOS.

Nitric oxide synthases (NOSs) catalyze the oxidation of L-arginine to nitric oxide (NO) and L-citrulline (*1*). Mammals contain three NOS isoforms: neuronal NOS (nNOS), inducible NOS (iNOS), and endothelial NOS (eNOS) (*2*). NO produced from these different NOS isoforms is involved in a wide range of physiologic functions in the nervous, immune, and cardiovascular systems (*3*). Unregulated NO production can lead to pathologic conditions such as stroke (*4*), inflammation (*5*), and hypertension (*6*). Therefore, the control of NOS activity by isoform-selective NOS inhibitors has great potential for therapeutic treatments of NO-related diseases (*7*).

[†]This work was supported by National Institutes of Health Grants GM57353 (T.L.P.) and GM49725 (R.B.S.).

[‡]Protein Data Bank entries 3N5V for nNOS−**3h**, 3N5W for nNOS−**3j**, 3N5X for nNOS−**3k**, 3N5Y for nNOS−**3l**, 3N5Z for nNOS−**3m**, 3N60 for nNOS−**3n**, 3N62 for nNOS D597N−**3j**, 3N64 for nNOS D597N−**3n**, 3N61 for nNOS D597N/M336V−**3j**, 3N63 for nNOS D597N/M336V−**3n**, 3N65 for nNOS S602H−**3j**, 3N66 for nNOS S602H−**3n**, 3N5R for eNOS−**3h**, 3N5T for eNOS−**3j**, 3N5S for eNOS−**3k**, 3N5P for eNOS−**3m**, 3N5Q for eNOS−**3n**, 3N6F for eNOS N368D−**3j**, 3N6G for eNOS N368D−**3k**, 3N6E for eNOS N368D−**3n**, 3N68 for eNOS N368D/V106M−**3h**, 3N69 for eNOS N368D/V106M−**3j**, 3N6A for eNOS N368D/V106M−**3k**, 3N67 for eNOS N368D/V106M−**3n**, 3N6B for eNOS H373S−**3j**, 3N6C for eNOS H373S−**3m**, and 3N6D for eNOS H373S−**3n**.

*To whom correspondence should be addressed. T.L.P.: e-mail, poulos@uci.edu; phone, (949) 824-7020; fax, (949) 824-3280. R.B.S.: e-mail, Agman@chem.northwestern.edu; phone, (847) 491-5653; fax, (847) 491-7713.

The three NOS isoforms share a similar domain architecture with an N-terminal catalytic domain containing the heme active site and a tetrahydrobiopterin (H_4B) nearby as a redox active cofactor and a C-terminal reductase domain consisting of FMN, FAD, and NADPH binding sites (*8*). The active sites for the various NOS isoforms, however, are nearly identical, which has presented a serious challenge in the development of isoform-selective inhibitors. Nevertheless, we found (*9*) that a single amino acid difference between nNOS and eNOS, Asp597 in nNOS versus Asn368 in eNOS, is responsible for why a series of dipeptide amide inhibitors (*10*−*12*) bind much more tightly to nNOS than eNOS. In this earlier work, we observed that a series of dipeptide amide inhibitors bind quite differently in eNOS and nNOS. In nNOS, the inhibitors adopt a "curled" conformation that allows the didpeptide amide α-amino group to be in position to interact with Asp597. However, in eNOS, the dipeptide amide inhibitors adopt an extended conformation because Asp597 is replaced with Asn368 in eNOS, and thus, there is no additional electrostatic incentive in eNOS for the inhibitors to "curl". The N368D mutant of eNOS and the D697N mutant of nNOS confirmed that the Asn versus Asp difference is the primary structural basis for why the dipepetide amide inhibitors bind much better to nNOS (*9*). This led to the design of a series of chiral pyrrolidine inhibitors (Figure 1) that exhibit K_i values in the low nanomolar range, with some exhibiting up to 4000-fold selectivity for nNOS

Published on Web 10/30/2010

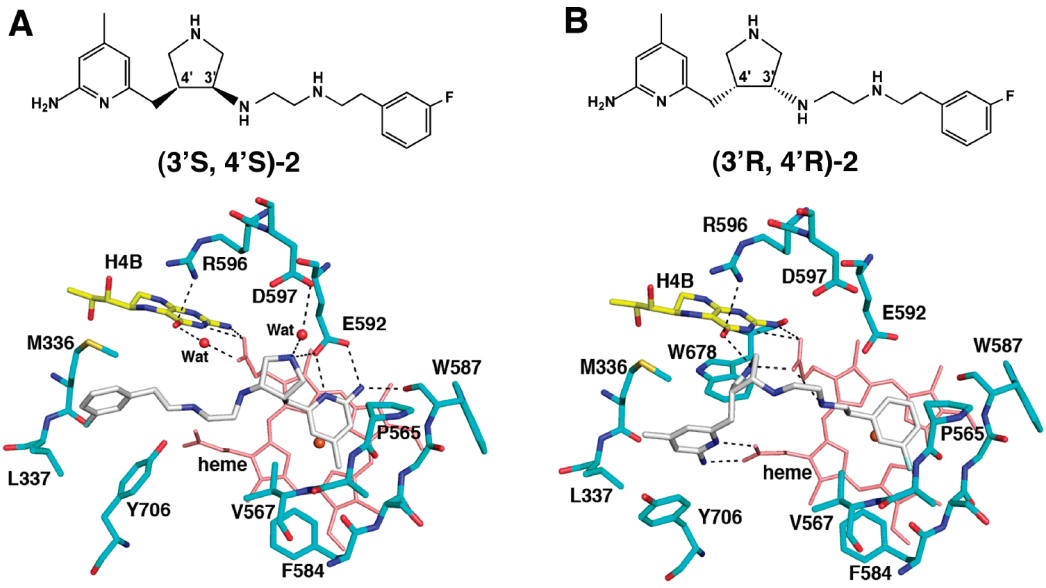

FIGURE 1: Two different binding orientations of *cis*-pyrrolidine compounds. (A) The aminopyridine of (3′*S*,4′*S*)-**2** interacts (---) with Glu592, while (B) the aminopyridine of (3′*R*,4′*R*)-**2** is flipped and interacts with heme propionate D. All of the structural figures were prepared with PyMOL (www.pymol.org).

over eNOS (*13*−*16*). The most potent of these inhibitors have dramatic in vivo effects and can protect newborn rabbit kits from experimentally induced ischemic brain damage (*14*).

We had anticipated that these pyrrolidine inhibitors would bind so that the aminopyridine group would mimic the substrate L-Arg guanidinium and be situated over the heme and hydrogen bond/ion pair with the active site Glu592. Indeed, this is the case for the (3′*S*,4′*R*) and (3′*R*,4′*S*)-*trans* inhibitors and the (3′*S*,4′*S*)-*cis* inhibitors [e.g., (3′*S*,4′*S*)-**2** (Figure 1A)] whose structures were determined in a previous study (*17*). However, the crystal structures (*17*) showed that (3′*R*,4′*R*)-*cis* compounds [e.g., (3′*R*,4′*R*)-**2**] bind with the inhibitor flipped 180° so that the "tail" fluorophenyl end is situated over the heme, leaving the aminopyridine in position to hydrogen bond/ion pair with heme propionate D (Figure 1B). Binding in the flipped orientation requires the movement of Tyr706. Because the aminopyridine portion of the inhibitor can bind in two flipped orientations, we reasoned that a symmetric, "double-headed" inhibitor that has an aminopyridine at each end should bind especially well, displacing Tyr706 for direct interactions between one aminopyridine and the heme propionate and the other aminopyridine with Glu592. A series of double-headed inhibitors now have been designed and synthesized, and their K_i values have been measured (*18*). Here we report the crystal structures of these inhibitors bound to both nNOS and eNOS.

MATERIALS AND METHODS

Inhibitor Design, Syntheses, and in Vitro Inhibitory Assay. The design, syntheses, and structure−activity relationship studies of the double-headed aminopyridine inhibitors have been reported elsewhere (*18*). K_i values and the selectivity for the best of the inhibitors used in this study are summarized in Table 1.

Protein Preparation and Crystallization. The nNOS S602H and eNOS H373S mutants were prepared using the QuikChange mutagenesis kit from Stratagene. The single point mutation was introduced into the wild-type full-length nNOS or eNOS coding sequence in the pCWori plasmid according to the manufacturer's instructions. The mutation sites were confirmed by DNA sequencing. The nNOS or eNOS heme domain proteins, wild type or mutants, used for crystallographic studies were produced by limited trypsin digestion from the corresponding full-length enzymes and further purified through a Superdex 200 gel filtration column (GE Healthcare), as described previously (*9*, *19*). The enzyme−inhibitor complex crystals were obtained by soaking rather than cocrystallization as reported in the earlier structural work (*9*). The nNOS heme domain at 7−9 mg/mL containing 20 mM histidine or the eNOS heme domain at 20 mg/mL with 2 mM imidazole was used for the sitting drop vapor diffusion crystallization setup under the conditions reported previously (*19*, *20*). Fresh crystals (1−2 days old) were first passed stepwise through cryo-protectant solutions described previously (*19*, *20*) and then soaked with 10 mM inhibitor (1.5 mM Zn^{2+} acetate was included in soaks for eNOS) for 4−6 h at 4 °C before being flash-cooled by being plunged into liquid nitrogen. Crystals were stored in liquid nitrogen until data could be collected.

Identification of the Metal Site with Anomalous Difference Fourier Techniques. The new metal site discovered in the nNOS−**3j** or nNOS−**3n** complex structure is surrounded by Asp600, His692 (subunit B), the pyridine nitrogen of **3j** (a chlorine anion in the case of the nNOS−**3n** complex), and a solvent molecule with tetrahedral geometry. The strong difference density at 15σ and the coordination geometry indicate a site for the first row transition metal ions. We identified the unknown metal using anomalous difference Fourier techniques similar to those we used to identify the native Zn^{2+} site while determining the initial crystal structure of eNOS (*20*). Fluorescence scans were performed with nNOS-**3n** crystals at Stanford Synchrotron Radiation Lightsource (SSRL) beamline 9-2 near the X-ray absorption edges of Fe, Co, Ni, Cu, and Zn. The absorption signals were detected at the edges of Fe, Cu, and Zn. The anomalous diffraction data were collected at two wavelengths for each of the three metals, one at the peak position of the absorption edge (e.g., E_1 = 9667 eV for Zn) and the other 60−80 eV from the edge toward the low-energy side (E_2 = 9600 eV for Zn). To measure the anomalous signals accurately, we used an inverse beam data collection protocol with a 10° wedge size and a

Table 1: K_i Values (*18*) and Selectivity of Inhibitors Used in This Study

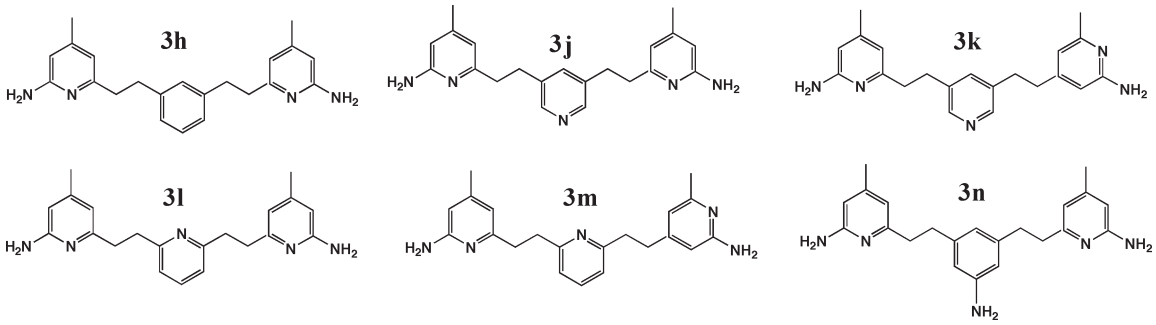

compound	[nNOS] (nM)	[eNOS] (nM)	[iNOS] (nM)	n/e[a]	n/i[a]
3h	38	4200	2730	111	71.8
3j	25	2680	1450	107	58
3k	103	16100	1910	156	19
3l	99	9400	4750	95	48
3m	195	20000	12600	102	64
3n	85	4950	3400	58	40

[a]The ratio of K_i (eNOS or iNOS) to K_i (nNOS).

Table 2: Anomalous Data Collection Statistics for nNOS−**3n** Complex Crystals

	Zn E_1	Zn E_2	Fe E_1	Fe E_2	Cu E_1	Cu E_2
X-ray wavelength (Å)	1.28249	1.29146	1.73875	1.75361	1.37786	1.38835
X-ray energy (eV)	9667	9600	7130	7070	8998	8930
resolution (Å)	2.80 (2.87−2.80)	2.80 (2.87−2.80)	2.95 (3.02−2.95)	2.95 (3.02−2.95)	2.85 (2.92−2.85)	2.85 (2.92−2.85)
R_{merge}	0.075 (0.51)	0.076 (0.49)	0.089 (0.60)	0.090 (0.64)	0.082 (0.53)	0.082 (0.52)
$I/\sigma I$	18.9 (3.0)	18.8 (2.9)	15.0 (2.0)	15.7 (2.0)	17.0 (2.4)	16.8 (2.4)
no. of unique reflections	44318	44290	38273	38583	42589	42007
completeness (%)	98.7 (99.7)	98.6 (98.2)	99.0 (96.4)	98.9 (95.4)	98.3 (93.4)	98.4 (94.3)
redundancy	3.9 (3.8)	3.9 (3.6)	3.8 (3.4)	3.8 (3.2)	3.9 (3.4)	3.9 (3.3)

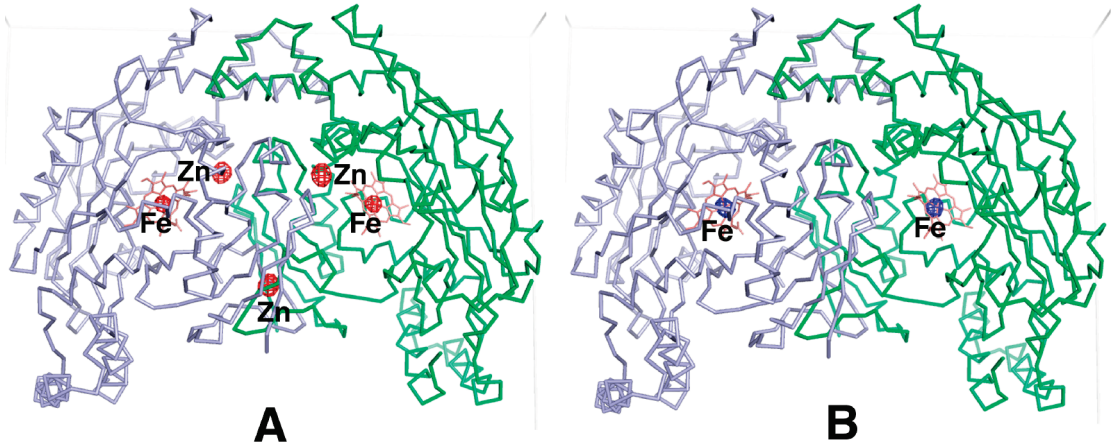

FIGURE 2: Display of the anomalous difference density of a nNOS crystal bound with **3n** at the 5σ contour level calculated at (A) the Zn absorption edge (9667 eV, 1.28 Å) and (B) 67 eV from the edge on the low-energy side (9600 eV, 1.29 Å). The Zn peaks disappeared in panel B because of the weak anomalous signal of Zn at the X-ray wavelength of 1.29 Å, but the anomalous signals from the two heme iron atoms persist.

2 s exposure time per frame (1° in scanning Φ angle). For each metal, two anomalous data sets at E_1 and E_2 were processed separately with HKL2000 (*21*). The anomalous data collection statistics collected at the Zn, Fe, and Cu edges are summarized in Table 2. To conduct the anomalous difference Fourier map calculation using FFT in CCP4 (*22*), we obtained the model phases by running a rigid body refinement with REFMAC (*23*) of the known nNOS heme domain model against each of the new anomalous data sets (E_1 or E_2), and the Fourier coefficient was the anomalous difference [$\Delta F = F(+) - F(-)$]. There is one homodimer in the asymmetric unit of the nNOS structure. The resulting maps (Figure 2) for Zn edge data showed five peaks above 10σ (the noise peaks were all below 5σ) at E_1, consisting of the native Zn, two new metal sites, and two heme sites, while only

Table 3: Crystallographic Data Collection and Refinement Statistics (part 1)[a]

	nNOS−**3j**	nNOS−**3l**	nNOS−**3n**	nNOS D597N−**3j**	nNOS D597N/M336V−**3j**	eNOS−**3j**	eNOS−**3n**
			Data Collection				
PDB entry	3N5W	3N5Y	3N60	3N62	3N61	3N5T	3N5Q
space group	$P2_12_12_1$	$P2_12_12_1$	$P2_12_12_1$	$P2_12_12_1$	$P2_12_12_1$	$P2_12_12_1$	$P2_12_12_1$
cell dimensions [*a*, *b*, *c* (Å)]	52.3, 111.2, 164.8	51.7, 110.6, 164.1	51.9, 111.2, 164.0	51.8, 110.4, 164.1	51.8, 110.5, 164.3	58.1, 106.7, 157.4	57.9, 107.1, 157.3
resolution (Å)	1.73 (1.76−1.73)	2.05 (2.09−2.05)	1.98 (2.01−1.98)	1.95 (1.98−1.95)	1.95 (1.98−1.95)	2.52 (2.56−2.52)	3.00 (3.05−3.00)
R_{sym} or R_{merge}	0.051 (0.59)	0.066 (0.56)	0.054 (0.64)	0.069 (0.58)	0.066 (0.50)	0.083 (0.559)	0.135 (0.638)
$I/\sigma I$	29.1 (2.1)	21.2 (1.9)	28.7 (2.1)	21.5 (2.4)	21.1 (1.8)	15.0 (1.9)	9.7 (2.1)
no. of unique reflections	101279	60097	67020	69795	69511	33841	19856
completeness (%)	99.5 (99.8)	99.4 (94.6)	99.4 (89.8)	99.8 (100.0)	99.7 (98.4)	99.8 (99.8)	97.9 (99.1)
redundancy	4.0 (4.0)	4.0 (3.7)	4.5 (4.2)	4.0 (4.1)	4.0 (3.8)	3.6 (3.6)	4.0 (4.0)
			Refinement				
resolution (Å)	1.73	2.05	1.98	1.95	1.95	2.52	3.00
no. of reflections used	95347	56712	63638	66262	65998	32111	18829
R_{work}/R_{free}[b]	0.182/0.205	0.184/0.228	0.191/0.232	0.173/0.208	0.179/0.213	0.186/0.248	0.181/0.269
no. of atoms							
protein	6678	6658	6659	6700	6699	6429	6413
ligand/ion	205	182	145	275	192	199	181
water	594	358	347	398	403	138	43
root-mean-square deviations							
bond lengths (Å)	0.012	0.012	0.015	0.013	0.013	0.014	0.016
bond angles (deg)	1.241	1.316	1.476	1.393	1.352	1.531	1.620

[a]See Table 1 for the nomenclature and chemical formula of inhibitors. [b]Five percent of reflections has been set aside during the entire course of refinement for the R_{free} calculation only. For each NOS isoform, the choice of R_{free} flags has been kept the same as those used in the starting model.

two peaks (two heme sites) were at E_2. The disappearance of the anomalous signals from the native Zn and the two new metal sites at wavelength E_2 (where the f'' of Zn is less than 0.5 electron) indicated that the unknown metal at the new site is Zn. The anomalous data collected at the Fe edge confirmed that the Fe is located at the two heme sites only, while the data for Cu detected no specific Cu binding site in the structure (data not shown). The Cu fluorescence signals shown during the scan may represent the random binding of the metal in solvent channels of the crystal lattice.

Collection and Processing of X-ray Diffraction Data and Structure Refinement. The cryogenic (100 K) X-ray diffraction data were collected remotely at various beamlines at SSRL through data collection control software Blu-Ice (*24*) and the crystal mounting robot. Raw data frames were indexed, integrated, and scaled using HKL2000 (*21*). Typically, each data set consisted of 90−100° of data with a 0.5° frame width for both nNOS and eNOS crystals because of their identical orthorhombic $P2_12_12_1$ space group symmetry.

The binding of inhibitors was detected by the initial difference Fourier maps calculated with CNS (*25*). The inhibitor molecules were then modeled in O (*26*) or COOT (*27*) and refined using CNS. Refinements were continued with REFMAC (*23*) to implement the TLS (*28*) protocol with each subunit as one TLS group. Water molecules were added and checked by COOT. The sigmaA-weighted omit $F_o - F_c$ electron density maps were calculated with REFMAC by running TLS + Restrained refinement with the interested ligand(s) omitted from the coordinate file. The refined structures were validated through COOT as well as the RCSB validation server with no outlier in the Ramachandran plot. The crystallographic data collection and structure refinement statistics are summarized in Table 3 and Table S1 of the Supporting Information. Coordinates of all the crystal structures reported in this work have been deposited in the RCSB Protein Data Bank (PDB).

RESULTS AND DISCUSSION

*Discovery of a New Zn^{2+} Site upon Binding of **3j** (**3k**) to nNOS*. The basic idea behind the double-headed inhibitors is for one aminopyridine to bind in the active site and interact with Glu592 while the second extends out of the active site, displaces Tyr706, and interacts with heme propionate D. The inhibitory constants (K_i) of these compounds have been determined (*18*), and the results relevant to this study are summarized in Table 1. Some of these compounds also exhibited IC_{50} values in the 5 μM range in cell-based assays, thus indicating the potential for in vivo applications (*18*).

To determine if our expectation of how these inhibitors should bind was correct, we determined crystal structures of nNOS and eNOS in complex with compounds that exhibited good inhibitory potency. Compound **3j** (Table 1) binds as expected with both aminopyridine rings involved in hydrogen bonding interactions with Glu592 and the heme (Figure 3). Quite unexpectedly, however, a second molecule of **3j** (**3jB**) binds with one aminopyridine group situated in the H_4B binding pocket. Moreover, there is strong difference density (15σ) near the bridging pyridine nitrogen atom of **3jB**. The electron density also is near Asp600 and His692 of subunit B (His692B) in the nNOS dimer. These two residues, the **3j** pyridine, and a large solvent ion (probably chloride) are tetrahedrally arranged around the large lobe of density highly reminiscent of a metal binding site. To determine the identity of the metal ion, we collected a series of data sets at different wavelengths near the absorption edge of the most likely metal candidates (Zn^{2+}, Cu^{2+}, Fe^{3+}/Fe^{2+}, Ni^{2+}, and Co^{2+}) as well at 50−80 eV lower energies from each metal absorption edge. Using this method, the metal bound was unambiguously identified as Zn^{2+} (Figure 2 and Table 2).

Zinc was not included during purification or crystallization, so the source of zinc remains unclear. NOS dimerizes through the heme domain with a Zn^{2+} coordinated to four Cys residues at the

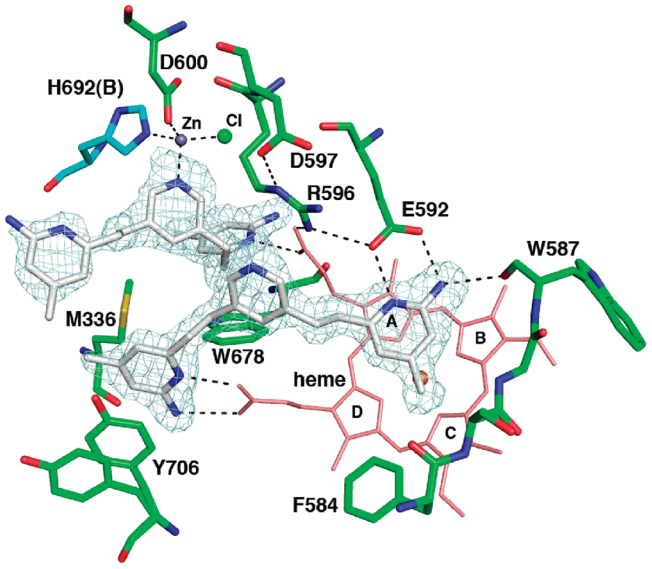

FIGURE 3: nNOS active site with one molecule of **3j** bound above the heme and the other in the pterin binding pocket. The sigmaA-weighted $F_o - F_c$ omit density map for **3j** is shown at a 3.0σ contour level. The ligation bonds around the new Zn^{2+} site and hydrogen bonds are depicted with dashed lines. Two alternate side chain conformations are shown for residue Tyr706. NOS dimerizes through the heme domains with the pterin binding in a pocket at the dimer interface. Residues of subunit A are depicted with green bonds and those of subunit B with cyan bonds. Four pyrrole rings of heme are labeled.

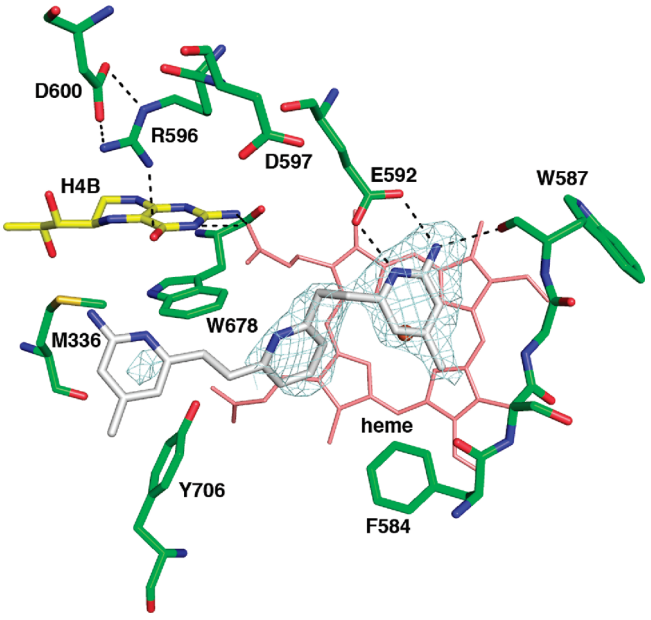

FIGURE 4: nNOS active site with one molecule of **3l** bound above the heme. The sigmaA-weighted $F_o - F_c$ omit density map for **3l** is shown at a 3.0σ contour level. Major hydrogen bonds are depicted with dashed lines. The second aminopyridine is partially disordered.

dimer interface. If we assume this dimer interface Zn^{2+} is at full occupancy, then the new Zn^{2+} site has an occupancy of ≈0.7. For Zn^{2+} to bind, substantial conformational rearrangements must occur in addition to displacement of the H_4B by **3j**B. The Arg596 side chain, which H-bonds with the H_4B, must swing out of the way and adopts a new conformation where it now forms hydrogen bonds to both Glu592 and Asp597 (Figure 3). The imidazole ring of His692B rotates 180° to allow the NE2 atom to provide one of the Zn^{2+} ligands. This also requires a slight movement of His692B toward the new Zn^{2+} site, resulting in a tightening of the dimer interface. This new ring orientation of His692B is only possible when Arg596 swings out of the way. Another inhibitor analogous to **3j**, namely **3k**, which has its aminopyridine ring nitrogen located at a different position (Table 1), shows a structure with two inhibitors bound nearly identical to that of **3j** (Figure S1A of the Supporting Information).

Structural Requirements for Zn^{2+} Binding. We next explored the structural requirements for the novel Zn^{2+} site. Because the bridging pyridine N atom of **3j**B provides a Zn^{2+} ligand, then its removal should prevent Zn^{2+} binding. Compound **3h**, with the bridging pyridine replaced with a benzene ring, binds with one molecule at the substrate binding site without a second molecule that replaces the H_4B, and there is no new Zn^{2+} site found with this inhibitor (Figure S1B of the Supporting Information). We next asked if how the bridging pyridine is attached to the two aminopyridines is important. The nNOS−**3j** structure indicates that attachment of the aminopyridines to the bridging pyridine at the *meta* positions is the only way to properly position the pyridine nitrogen for Zn^{2+} coordination. To test this idea, an analogue of **3j**, **3l** (Table 1), was synthesized that has its nitrogen atom in the bridging pyridine adjacent (*ortho*) to the two substituents. As expected, there is no second molecule of **3l** bound to nNOS (Figure 4). The H_4B remains bound, and therefore, no new Zn^{2+} site is found. However, the first molecule of **3l** is not bound to nNOS in the same way as **3j**. The interaction between the new pyridine nitrogen of **3l** and heme propionate A moves the second aminopyridine out of position for interaction with heme propionate D (Figure 4). A structural analogue of **3l**, namely **3m** (Table 1), gives a similar structure with one inhibitor bound (Figure S2 of the Supporting Information).

While testing the variations at the bridging ring of these double-headed aminopyridine compounds, we found one of the inhibitors, **3n** (Table 1), with an aniline group as the bridging ring, leads to a structure with even more surprising results. This time, only one inhibitor is bound, with its first aminopyridine interacting with Glu592 as usual, but with its second aminopyridine directly replacing the H_4B and stacking against the Trp678 side chain (Figure 5). Because the H_4B is no longer in place and the Arg596 side chain swings out, the same new Zn^{2+} site is created. The only difference with the Zn^{2+} site seen in the nNOS−**3j** structure is the fact that the inhibitor **3n** is not part of the Zn^{2+} coordination sphere. Rather, a chloride ion and a water molecule are the metal ligands in addition to the side chains of Asp600 and His692 (subunit B). The binding of **3n** causes the largest distortion to the heme propionate (pyrrole A) so far observed in any available nNOS inhibitor complex structure. This propionate is now hydrogen bonded to the side chain of Arg596 in its new rotamer position (Figure 5). The same heme propionate is important to H_4B binding because of hydrogen bonding interactions. Any distortion of this propionate position would cause the weakening of cofactor binding, which is the common feature we have found in the nNOS complex structures with **3j**, **3k**, and **3n**. To briefly summarize, our results thus far indicate that the key to forming the new Zn^{2+} site is the movement of Arg596, which provides room for a Zn^{2+} ion to bind and coordinate with Asp600 and His692 from subunit B.

No Zn^{2+} Site Found in eNOS. Although these double aminopyridine compounds bind to eNOS with only micromolar affinity, it was important to determine if inhibitors such as **3j**, **3k**, and **3n**, which are capable of creating the new Zn^{2+} binding site in

nNOS, can do the same to eNOS. Even though the Zn^{2+} coordinating residues in nNOS, Asp600 and His692B, are conserved in eNOS, Asp371 and His463B, respectively, we did not detect any trace of Zn^{2+} binding in eNOS structures, even after inclusion of 1.5 mM Zn^{2+} in the cryosoaks (Figure 6A). Only one molecule of **3j** binds, as in the nNOS−**3jA** complex, but there is no disturbance of the heme propionate or Arg367 as when the second **3jB** molecule binds to nNOS. As with the nNOS−**3n** complex, only one **3n** molecule binds to eNOS, but the second aminopyridine of **3n** adopts a substantially different conformation than in nNOS (Figure 6B). The first aminopyridine of **3n** interacts with Glu363, the same as in nNOS, but the bridging aniline ring does not press against heme propionate A, resulting in a repositioning of the heme propionate as in nNOS. Instead, it is situated between the two heme propionate groups and does not result in any change in the heme propionate. In addition, Arg367 does not move, H_4B remains bound, and thus Zn^{2+} cannot bind.

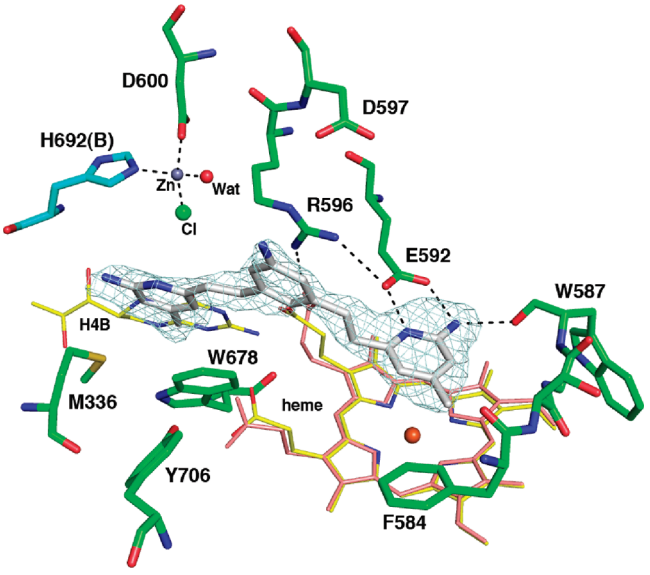

FIGURE 5: nNOS active site with compound **3n** bound. The $F_o - F_c$ omit electron density for the inhibitor is contoured at 3.0σ. The ligation bonds of the new Zn^{2+} site and hydrogen bonds are depicted with dashed lines. The heme and H_4B in the substrate-bound structure (PDB entry 1OM4) are overlaid to illustrate the large conformational change of heme propionate A and the displacement of H_4B by the second aminopyridine of the inhibitor.

The most obvious difference between nNOS and eNOS that might contribute to Zn^{2+} binding in nNOS is Asp597 in nNOS, which is Asn368 in eNOS. In nNOS, Arg596 must swing out of the way to H-bond with Asp597, and because eNOS has an Asn367 instead of Asp, there may not be the electrostatic energetic incentive for Arg367 to move in eNOS. Another difference between nNOS and eNOS that we have found contributes to selectivity in previous studies is Val106 in eNOS, which is Met336 in nNOS (*9*). However, a series of crystal structures of the eNOS N368D/V106M double mutant in complex with double-headed inhibitors shows that Arg367 remains in place, and thus, a second inhibitor molecule and Zn^{2+} cannot bind (Figures S3−S6 of the Supporting Information). We next examined the inverse mutation in nNOS and converted Asp597 to Asn. The D597N mutant binds **3n** the same as wild-type nNOS, which includes Zn^{2+} (Figure S7 of the Supporting Information). In the presence of **3n**, the Arg596 side chain still swings out in a position of hydrogen bonding to Asn597 even though the residue no longer bears a negative charge as Asp597 in wild-type nNOS. Clearly, the ability of Arg596 to move does not depend on ion pairing with Asp597.

Is Removal of H_4B Necessary in Creation of the Zn^{2+} Site? The next question addressed is whether displacement of H_4B is required for Zn^{2+} binding. The answer is no. In the nNOS D597N−**3j** complex, the first **3j** molecule binds to nNOS the same as in the wild type. However, the electron density for the second molecule is not well-defined and could best be accounted for by assuming partial occupancy for both the inhibitor and H_4B (Figure 7A). The new Zn^{2+} is still present, but one of the four ligands is either the partially occupied inhibitor or a partially occupied water molecule (Figure 7A). The heme propionate that must move when two inhibitors bind also exhibits partial occupancy in two different conformations. The picture becomes a little more complicated in the nNOS D597N/M336V double mutant (Met336 is Val in eNOS). In this mutant, only one **3j**

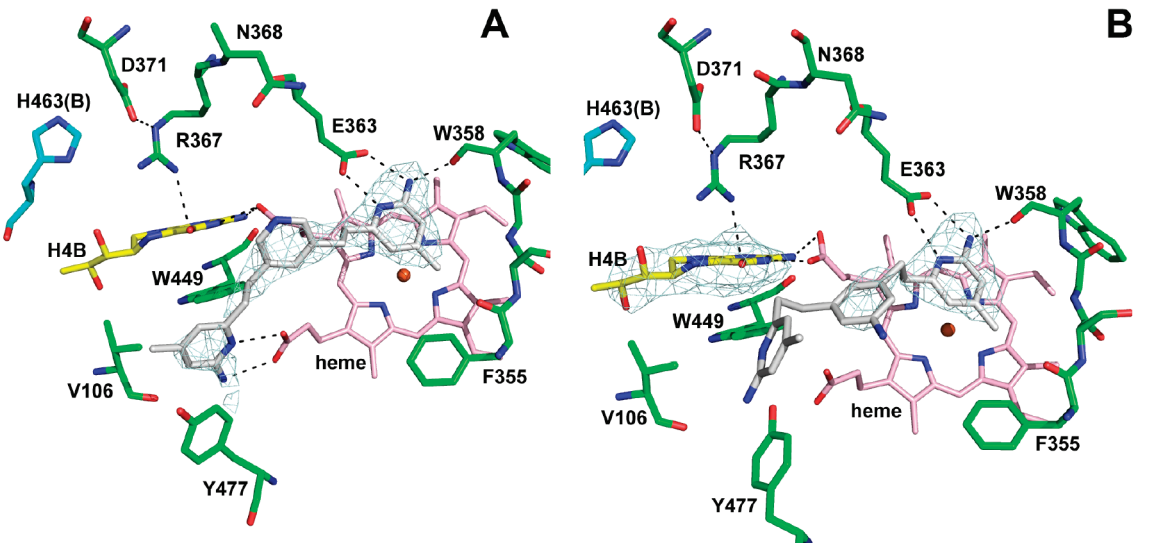

FIGURE 6: eNOS active site with compound **3j** (A) or **3n** (B) bound. The $F_o - F_c$ omit electron density for the inhibitor is contoured at 2.5σ. Hydrogen bonds are depicted with dashed lines. In panel A, Tyr477 moves to allow interaction of **3j** with the heme propionate. In panel B, the second aminopyridine of **3n** is partially disordered. The H_4B is not disturbed by ligand binding illustrated by the omit electron density for the pterin at 2.5σ.

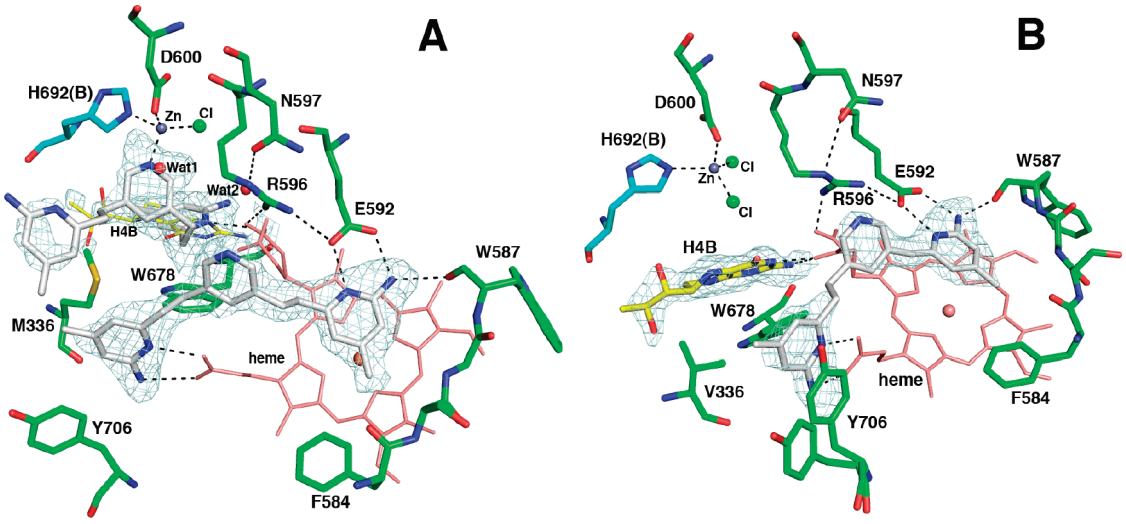

FIGURE 7: Active site of (A) nNOS D597N or (B) nNOS D597N/M336V with compound **3j** bound. The $F_o - F_c$ omit density map for the inhibitor is shown at a 2.5σ (A) or 3.0σ (B) contour level. The new Zn site ligation bonds and hydrogen bonds are drawn as dashed lines. Heme propionate A in each case has alternate conformations. In panel A, the second molecule of **3j** only partially occupies the pterin site, while H_4B together with two water molecules, Wat1 and Wat2, accounts for the rest. In panel B, there is no second **3j** molecule; hence, H_4B binds with full occupancy indicated by the $F_o - F_c$ omit density map at 3.0σ.

molecule is bound (Figure 7B). In the wild-type protein, the Met336 SD atom is 3.8 Å from inhibitor A and 4.4 Å from inhibitor B, the one that displaces H_4B. These interactions are lost when Met366 is changed to Val, thus decreasing the affinity for the second inhibitor molecule.

What Prevents eNOS from Binding a New Zn^{2+}? What remains a puzzle is why eNOS and the eNOS mutants designed to mimic nNOS fail to bind a second inhibitor molecule and thus do not bind Zn^{2+}. Upon further examination of the structures, one additional difference may be contributing. His373 in eNOS would be ~4.0 Å from inhibitor B (if it would have bound) and thus might interfere with binding. This residue is Ser602 in nNOS. However, the nNOS S602H mutant still binds two molecules of **3j** with Zn^{2+} bound, although inhibitor B and H_4B are at partial occupancy (Figure S8A of the Supporting Information). The nNOS S602H−**3n** structure shows one inhibitor bound that displaces the H_4B and also promotes the formation of the new Zn^{2+} site just like wild-type nNOS (Figure S8B of the Supporting Information). However, the inverse mutant in eNOS, H373S, binds **3j** and **3n** just like wild-type eNOS with only one inhibitor bound (Figure S9A,B of the Supporting Information). Therefore, the involvement of this His373 of eNOS in prevention of binding a new Zn^{2+} in eNOS has been ruled out.

While the various mutants do perturb the binding of the double-headed inhibitors, other more subtle factors that are not due to obvious amino acid differences near the inhibitors or Zn^{2+} control why nNOS can bind Zn^{2+} but not eNOS. Although the results we have obtained are somewhat complicated by the partial occupancy of inhibitor B in the nNOS mutants designed to mimic eNOS, there are three criteria that must be met in the formation of the new Zn^{2+} site. First, Arg596 must move from its H-bonding position with H_4B to make room for the Zn^{2+}. Second, the heme propionate A normally H-bonding with H_4B must move to make room for the second inhibitor that coordinates the Zn^{2+}. Third, one of the Zn^{2+} ligands, His692B, is from subunit B at the dimer interface. For His692B to coordinate Zn^{2+}, the His692B side chain must adopt a new rotamer conformation and move ~0.5 Å closer to subunit A, which requires some flexibility at the dimer interface. eNOS cannot undergo any of these changes required for binding of the second inhibitor and/or Zn^{2+}. It is well-known that the eNOS dimer is more stable than that of either nNOS or iNOS, indicating a more rigid and less flexible dimer interface in eNOS (*29*). Such rigidity could prevent the movement of His463B required to bind Zn^{2+}. In addition, a tighter interface may make it more difficult to disrupt the heme propionate−H_4B H-bonding interactions, which are required for binding of the second inhibitor molecule. Although not an easily testable hypothesis, the best explanation for the primary causal differences between eNOS and nNOS in binding these double-headed inhibitors is the more rigid dimer interface in eNOS along with the greater flexibility in nNOS, which allows the required motions needed for binding Zn^{2+}.

Significance for NOS Inhibitor Design. The significant conformational changes observed upon inhibitor binding and formation of the new Zn^{2+} site have identified three key flexible regions in nNOS, but not in eNOS, which may prove useful in the design of a new generation of NOS inhibitors. First, heme propionate A, which interacts with the H_4B, is quite flexible and adopts various conformations in response to the bulkiness and chemical nature of the ligand bound at the substrate binding pocket. The conformation of this heme propionate will, in turn, affect the binding of the H_4B cofactor. Second, Arg596 must move to provide room for the new Zn^{2+} ion. Because Arg596 interacts with the H_4B, movement of Arg596 and the heme propionate weakens H_4B binding, enabling easier displacement by the second inhibitor molecule. Third, we hypothesize that the relatively weaker dimer interface interactions in nNOS relative to eNOS allow one of the Zn^{2+} ligands, His692B, to move to optimize the Zn^{2+} coordination sphere. Because none of this occurs in eNOS, owing to of a more rigid dimer interface, it should be possible to exploit these nNOS-specific movements for novel nNOS-selective inhibitor design. With respect to selectivity, it is also worth noting that the new Zn^{2+} site is probably not "natural", because we observe the Zn^{2+} binding only in the presence of inhibitors. In no case was a Zn^{2+} ion found in either nNOS or eNOS crystals presoaked in the presence of either 10 mM arginine or 5 mM *S*-ethylisothiourea and 5 mM Zn^{2+} acetate for 4 h (unpublished observations).

ACKNOWLEDGMENT

We thank the beamline staff at Stanford Synchrotron Radiation Lightsource for their assistance during remote X-ray diffraction data collections.

SUPPORTING INFORMATION AVAILABLE

Tables of crystallographic statistics and supplementary figures. This material is available free of charge via the Internet at http://pubs.acs.org.

REFERENCES

1. Stuehr, D. J., and Griffith, O. W. (1992) Mammalian nitric oxide synthases. *Adv. Enzymol. Relat. Areas Mol. Biol. 65*, 287–346.
2. Knowles, R. G., and Moncada, S. (1994) Nitric oxide synthases in mammals. *Biochem. J. 298*, 249–258.
3. Moncada, S., and Higgs, E. A. (1991) Endogenous nitric oxide: Physiology, pathology and clinical relevance. *Eur. J. Clin. Invest. 21*, 361–374.
4. Sims, N. R., and Anderson, M. F. (2002) Mitochondrial contributions to tissue damage in stroke. *Neurochem. Int. 40*, 511–526.
5. Nathan, C. (1997) Inducible nitric oxide synthase: What difference does it make? *J. Clin. Invest. 100*, 2417–2423.
6. Taddei, S., Virdis, A., Ghiadoni, L., Sudano, I., and Salvetti, A. (2001) Endothelial dysfunction in hypertension. *J. Cardiovasc. Pharmacol. 38* (Suppl. 2), S11–S14.
7. Hobbs, A. J., Higgs, A., and Moncada, S. (1999) Inhibition of nitric oxide synthase as a potential therapeutic target. *Annu. Rev. Pharmacol. Toxicol. 39*, 191–220.
8. Alderton, W. K., Cooper, C. E., and Knowles, R. G. (2001) Nitric oxide synthases: Structure, function and inhibition. *Biochem. J. 357*, 593–615.
9. Flinspach, M. L., Li, H., Jamal, J., Yang, W., Huang, H., Hah, J. M., Gomez-Vidal, J. A., Litzinger, E. A., Silverman, R. B., and Poulos, T. L. (2004) Structural basis for dipeptide amide isoform-selective inhibition of neuronal nitric oxide synthase. *Nat. Struct. Mol. Biol. 11*, 54–59.
10. Huang, H., Martasek, P., Roman, L. J., Masters, B. S., and Silverman, R. B. (1999) N^{ω}-Nitroarginine-containing dipeptide amides. Potent and highly selective inhibitors of neuronal nitric oxide synthase. *J. Med. Chem. 42*, 3147–3153.
11. Huang, H., Martasek, P., Roman, L. J., and Silverman, R. B. (2000) Synthesis and evaluation of peptidomimetics as selective inhibitors and active site probes of nitric oxide synthases. *J. Med. Chem. 43*, 2938–2945.
12. Hah, J. M., Roman, L. J., Martasek, P., and Silverman, R. B. (2001) Reduced amide bond peptidomimetics. (4S)-N-(4-Amino-5-[aminoakyl]aminopentyl)-N′-nitroguanidines, potent and highly selective inhibitors of neuronal nitric oxide synthase. *J. Med. Chem. 44*, 2667–2670.
13. Ji, H., Stanton, B. Z., Igarashi, J., Li, H., Martasek, P., Roman, L. J., Poulos, T. L., and Silverman, R. B. (2008) Minimal pharmacophoric elements and fragment hopping, an approach directed at molecular diversity and isozyme selectivity. Design of selective neuronal nitric oxide synthase inhibitors. *J. Am. Chem. Soc. 130*, 3900–3914.
14. Ji, H., Tan, S., Igarashi, J., Li, H., Derrick, M., Martasek, P., Roman, L. J., Vasquez-Vivar, J., Poulos, T. L., and Silverman, R. B. (2009) Selective neuronal nitric oxide synthase inhibitors and the prevention of cerebral palsy. *Ann. Neurol. 65*, 209–217.
15. Igarashi, J., Li, H., Jamal, J., Ji, H., Fang, J., Lawton, G. R., Silverman, R. B., and Poulos, T. L. (2009) Crystal structures of constitutive nitric oxide synthases in complex with de novo designed inhibitors. *J. Med. Chem. 52*, 2060–2066.
16. Lawton, G. R., Ralay Ranaivo, H., Chico, L. K., Ji, H., Xue, F., Martasek, P., Roman, L. J., Watterson, D. M., and Silverman, R. B. (2009) Analogues of 2-aminopyridine-based selective inhibitors of neuronal nitric oxide synthase with increased bioavailability. *Bioorg. Med. Chem. 17*, 2371–2380.
17. Delker, S. L., Ji, H., Li, H., Jamal, J., Fang, J., Xue, F., Silverman, R. B., and Poulos, T. L. (2010) Unexpected binding modes of nitric oxide synthase inhibitors effective in the prevention of a cerebral palsy phenotype in an animal model. *J. Am. Chem. Soc. 132*, 5437–5442.
18. Xue, F., Delker, S. L., Li, H., Fang, J., Jamal, J., Martásek, P., Roman, L. J., Poulos, T. L., and Silverman, R. B. (2010) Symmetric double-headed aminopyridines, a novel strategy for potent and membrane-permeable inhibitors of neuronal nitric oxide synthase, *J. Med. Chem.* (submitted for publication).
19. Li, H., Shimizu, H., Flinspach, M., Jamal, J., Yang, W., Xian, M., Cai, T., Wen, E. Z., Jia, Q., Wang, P. G., and Poulos, T. L. (2002) The novel binding mode of N-alkyl-N′-hydroxyguanidine to neuronal nitric oxide synthase provides mechanistic insights into NO biosynthesis. *Biochemistry 41*, 13868–13875.
20. Raman, C. S., Li, H., Martasek, P., Kral, V., Masters, B. S., and Poulos, T. L. (1998) Crystal structure of constitutive endothelial nitric oxide synthase: A paradigm for pterin function involving a novel metal center. *Cell 95*, 939–950.
21. Otwinowski, Z., and Minor, W. (1997) Processing of X-ray diffraction data collected in oscillation mode. *Methods Enzymol. 276*, 307–326.
22. Collaborative Computational Project Number 4 (1994) The CCP4 Suite: Programs for Protein Crystallography. *Acta Crystallogr. D50*, 760–763.
23. Murshudov, G. N., Vagin, A. A., and Dodson, E. J. (1997) Refinement of Macromolecular Structures by the Maximum-Likelihood Method. *Acta Crystallogr. D53*, 240–255.
24. McPhillips, T. M., McPhillips, S. E., Chiu, H. J., Cohen, A. E., Deacon, A. M., Ellis, P. J., Garman, E., Gonzalez, A., Sauter, N. K., Phizackerley, R. P., Soltis, S. M., and Kuhn, P. (2002) Blu-Ice and the Distributed Control System: Software for data acquisition and instrument control at macromolecular crystallography beamlines. *J. Synchrotron Radiat. 9*, 401–406.
25. Brunger, A. T., Adams, P. D., Clore, G. M., DeLano, W. L., Gros, P., Grosse-Kunstleve, R. W., Jiang, J.-S., Kuszewski, J., Nilges, M., Pannu, N. S., Read, R. J., Rice, L. M., Simonson, T., and Warren, G. L. (1998) Crystallography & NMR System: A new software suite for macromolecular structure determination. *Acta Crystallogr. D54*, 905–921.
26. Jones, T. A., Zou, J.-Y., Cowan, S. W., and Kjeldgaarrd, M. (1991) Improved methods for building models in electron density and the location of errors in these models. *Acta Crystallogr. A47*, 110–119.
27. Emsley, P., Lohkamp, B., Scott, W., and Cowtan, K. (2010) Features and development of Coot. *Acta Crystallogr. D66*, 486–501.
28. Winn, M. D., Isupov, M. N., and Murshudov, G. N. (2001) Use of TLS parameters to model anisotropic displacements in macromolecular refinement. *Acta Crystallogr. D57*, 122–133.
29. Panda, K., Rosenfeld, R. J., Ghosh, S., Meade, A. L., Getzoff, E. D., and Stuehr, D. J. (2002) Distinct dimer interaction and regulation in nitric-oxide synthase types I, II, and III. *J. Biol. Chem. 277*, 31020–31030.